Multimodel Kalman filtering for adaptive nonuniformity correction in infrared sensors

Jorge E. Pezoa and Majeed M. Hayat

Department of Electrical and Computer Engineering, University of New Mexico, Albuquerque, New Mexico 87131-1356

Sergio N. Torres

Department of Electrical Engineering, University of Concepcion, Casilla 160-C, Concepcion, Chile

Md. Saifur Rahman

Department of Electrical Engineering, Indian Institute of Technology, Kharagpur, India

Received July 29, 2005; accepted November 18, 2005; posted December 9, 2005 (Doc. ID 63710)

We present an adaptive technique for the estimation of nonuniformity parameters of infrared focal-plane arrays that is robust with respect to changes and uncertainties in scene and sensor characteristics. The proposed algorithm is based on using a bank of Kalman filters in parallel. Each filter independently estimates state variables comprising the gain and the bias matrices of the sensor, according to its own dynamic-model parameters. The supervising component of the algorithm then generates the final estimates of the state variables by forming a weighted superposition of all the estimates rendered by each Kalman filter. The weights are computed and updated iteratively, according to the *a posteriori*-likelihood principle. The performance of the estimator and its ability to compensate for fixed-pattern noise is tested using both simulated and real data obtained from two cameras operating in the mid- and long-wave infrared regime. © 2006 Optical Society of America

OCIS codes: 100.2550, 040.1520, 110.3080, 100.3010, 100.3020.

1. INTRODUCTION

Today's infrared (IR) imaging systems predominantly employ focal-plane arrays (FPAs) of various technologies as their cores. Although FPAs have numerous advantages, such as compactness, production cost effectiveness, and high sensitivity, their discrete spatial structure brings about the notorious nonuniformity (NU) noise, also termed fixed-pattern noise (FPN), which affects the quality of the acquired imagery significantly from the radiometric and visual perspectives alike. NU noise is the pattern observed in the imagery when a spatially uniform input, such as a blackbody source, is imaged. This noise results from the spatial dissimilarities in the responses of the individual elements of the array, which is attributed to dissimilarities in the photodetectors' responsivities as well as pixel-to-pixel variations in the characteristics of the readout circuitry. Moreover, the level of NU noise varies depending on factors such as the surrounding temperature, the technology of the photodetector, and the readout architecture. Additionally, NU noise varies slowly over time, and, depending on the technology used, this drift can take from minutes to hours.[1] Therefore, a one-time laboratory (or factory) calibration of the FPA does not provide an effective solution to the NU problem; NU correction (NUC) must be performed repeatedly as drift occurs.

To date, several techniques have been proposed as suitable solutions to compensate for the NU in IR FPAs. The first group of them, known as calibration methods,[2–5] requires a known, spatially uniform reference scene in order to calibrate the responses of the elements of the FPA. Most of these techniques require the usage of flat scenes at two or more temperatures from a blackbody. This category of NUC techniques is often very precise and yields radiometrically accurate readouts. However, owing to the complexity of their setup, which requires the use of a blackbody source, electromechanical parts, and shutters and halting the operation of the camera during the period when calibration is conducted, they may not be practical in many imaging systems. These include systems that have weight or size constraints (e.g., airborne systems, portable systems) as well as systems that are designed to be functional at all times (e.g., surveillance systems).

The second group of NUC techniques are scene based, and they rely on signal processing to remove the NU noise. These include motion-based algorithms[6–10] and statistical algorithms.[1,11–17] Regardless of the specific algorithm employed, scene-based techniques require only the sequence of frames that is being imaged during the normal operation of the camera, and their performance is limited by the amount of information contained in the video sequence such as spatiotemporal diversity of the temperature in the scene[1,11–17] and the presence of global motion in the sequence.[6–10]

Of particular relevance to the technique developed in this paper is the algorithm developed by Torres and Hayat,[12] which employs a Gauss–Markov model for the NU parameters as a means to capture the drift in the

FPN. Their technique utilizes such dynamic model to estimate the gain and bias of each detector in the array from a video sequence by using a Kalman filter (KF). The KF assumes a known linear state-space dynamic model based on the known correlation in the gain and bias from one block of video sequence to the next. In practice, however, the parameters of the dynamic system may not be known exactly, or they may be known with some uncertainty. Therefore, system identification may be necessary to obtain the parameters of the dynamic system.

In this paper, a multimodel adaptive estimation (MMAE) approach is proposed and tested to estimate the gain and bias of each detector that allows for uncertainties in the level of drift in these NU parameters. The algorithm adopts a parallel-processing technique based on Kalman filtering, as described by Sims *et al.*[18] In particular, a bank of KFs is used to estimate the system states (viz., gain and bias), and the output residual errors of each estimate are used as hypotheses to test and assign *a posteriori* conditional probabilities to each model and KF. The algorithm updates these weights (as new blocks of video sequence arrive) for each KF and forms a linear composite estimate according to the weights.

This paper is organized as follows. In Section 2 the system model is presented, and the multimodel estimator is developed. In Section 3, the technique is tested using IR sequences corrupted by simulated NU noise. In Section 4, the technique is tested on real IR data using two cameras. The main conclusions are presented in Section 5.

2. ADAPTIVE MULTIMODEL ESTIMATION OF THE GAIN AND BIAS

We begin by reviewing germane aspects of the state-space dynamic model developed by Torres and Hayat,[12] which lays the foundation for the proposed adaptive Kalman-filtering technique. We then adopt the dynamic model and the form of the KF to develop the multimodel recursions for the adaptive estimation of the gain and bias.

A. State-Space Model

The detector's response is usually modeled as a first-order relationship between the input irradiance and the detector's output. For the (i,j)th detector in the FPA, the nth time sample of the input irradiance, $T^{ij}(n)$, is related to its corresponding output value $Y^{ij}(n)$ through the equation[11,19]

$$Y^{ij}(n) = A^{ij}T^{ij}(n) + B^{ij} + V^{ij}(n), \tag{1}$$

where A^{ij} is the gain of the (i,j)th pixel and B^{ij} is its bias. The term V^{ij} is the additive readout (temporal) noise associated with the (i,j)th detector. The main assumption in Eq. (1) is that no drift occurs in the gain and the bias within the time window used to collect the data. To simplify the notation, we will drop the pixel superscripts ij with the understanding that all operations are performed on a pixel-by-pixel basis.

Torres and Hayat[12] extended the model in Eq. (1) to consider drift in the gain and bias. In particular, they considered disjoint sequences of fixed-length vectors of detector readout values, called blocks of frames, and assumed that drift in the gain and bias occurs only when a block of frames arrives; i.e., the drift in the gain and the bias occurs only between blocks of observations. To do so, they employed a Gauss–Markov state-space dynamic model to characterize the drift in the gain and the bias. Mathematically, this model is given by[12]

$$\mathbf{X}_k = \mathbf{\Phi}\mathbf{X}_{k-1} + \mathbf{W}_k, \tag{2}$$

where $\mathbf{X}_k$ is the two-dimensional state vector comprising the gain A_k and the bias B_k at the kth block. The square diagonal matrix $\mathbf{\Phi}$ relates the transition between the states from one block to the next. The diagonal elements of $\mathbf{\Phi}$ are the parameters α and β that represent, respectively, the amount of drift in the gain and bias. The vector $\mathbf{W}_k$ is the driving noise vector of the Gauss–Markov model. The details on the selection of the mean and variance of $W_k^{(1)}$ and $W_k^{(2)}$, the components of $\mathbf{W}_k$, are discussed elsewhere.[12]

To complete the state-space dynamic model, we define the output vector, $\mathbf{Y}_k$, consisting of the readouts over each block of frames. This will constitute the observation equation for the state-space dynamic model, which is done by writing a vector form of Eq. (1) for each block of frames (and for each detector) in conjunction with the block-dependent biases and gains. More precisely,

$$\mathbf{Y}_k = \mathbf{H}_k\mathbf{X}_k + \mathbf{V}_k, \tag{3}$$

where $\mathbf{H}_k = [\mathbf{T}_k \;\; \mathbf{1}]$ is the observation matrix, $\mathbf{T}_k$ is a column vector of length l_k (l_k is the number of frames in the kth block) of the irradiance values in the kth block, and $\mathbf{1}$ is the all-ones vector of length l_k. The term $\mathbf{V}_k$ is the vector of independent, additive temporal noise elements in the kth block.

It is further assumed that the input irradiance values $\mathbf{T}_k$ in the kth block of frames are an independent sequence of uniformly distributed random variables in the range $[T^{\min}, T^{\max}]$. In particular, the range is common to all the detectors in each block of frames.[12] This is essentially one manifestation of the constant-statistics assumption proposed by Narendra,[11] which provides the statistical references according to which the gains and the biases are calibrated. In practice, this assumption is met when the block of frames exhibits sufficient irradiance diversity in the spatial domain. This can occur, for example, through motion in the camera whereby detectors are allowed to sense similar sets of irradiance values over the entire block of frames.

With the above state-space dynamic model, a KF was developed to estimate the gain and bias,[12] which is described by the following iterations:

$$\mathbf{P}_k^- = \mathbf{\Phi}\mathbf{P}_{k-1}\mathbf{\Phi}^T + \mathbf{Q}, \tag{4}$$

$$\mathbf{C}_k = \bar{\mathbf{H}}\mathbf{P}_k^-\bar{\mathbf{H}}^T + \mathbf{R} + \sigma_T^2(\sigma_{A_0}^2 + \bar{A}_0)\mathbf{I}_{l_k,l_k}, \tag{5}$$

$$\mathbf{K}_k = \mathbf{P}_k^-\bar{\mathbf{H}}^T\mathbf{C}_k^{-1}, \tag{6}$$

$$\mathbf{P}_k = (\mathbf{I}_{2,2} - \mathbf{K}_k\bar{\mathbf{H}})\mathbf{P}_k^-, \tag{7}$$

$$\hat{\mathbf{X}}_k^- = \mathbf{\Phi}\hat{\mathbf{X}}_{k-1} + \mathbf{M}, \tag{8}$$

$$\hat{\mathbf{X}}_k = \hat{\mathbf{X}}_k^- + \mathbf{K}_k(\mathbf{Y}_k - \bar{\mathbf{H}}\hat{\mathbf{X}}_k^-), \tag{9}$$

with the initial conditions

$$\hat{\mathbf{X}}_0 = \mathsf{E}[\mathbf{X}_0] = \begin{pmatrix} \bar{A}_0 \\ \bar{B}_0 \end{pmatrix}, \qquad \mathbf{P}_0 = \begin{bmatrix} \sigma_{A_0}^2 & 0 \\ 0 & \sigma_{B_0}^2 \end{bmatrix}. \tag{10}$$

In the above, $\hat{\mathbf{X}}_k^-$ and $\hat{\mathbf{X}}_k$ are, respectively, the *a priori* and the current-state estimates. The terms $\mathbf{P}_k^-$ and $\mathbf{P}_k$ are the *a priori* and the current error covariance matrices, respectively; $\mathbf{K}_k$ is the Kalman gain matrix, and $\mathbf{C}_k$ is the covariance matrix of the *a priori* output error residuals $\mathbf{r}_k \triangleq \mathbf{Y}_k - \hat{\mathbf{Y}}_k^-$, where $\hat{\mathbf{Y}}_k^- \triangleq \mathbf{H}_k \hat{\mathbf{X}}_k^-$. The matrix $\mathbf{R}$ is the covariance matrix of the additive noise, $\bar{\mathbf{H}}$ is the mean of the matrix $\mathbf{H}_k$, σ_T^2 is the common variance of the input irradiance, $\bar{A}_0(\bar{B}_0)$ and $\sigma_{A_0}^2(\sigma_{B_0}^2)$ are the mean and variance of the initial gain (bias), respectively, and, finally, the matrix $\mathbf{Q}$ is the covariance matrix of the driving noise vector. We use the notation $\mathbf{I}_{j,j}$ to represent the $j\times j$ identity matrix.

The above KF was designed under the assumption that the system parameters are known. These parameters include the gain and bias drift parameters, α and β, the common range of input irradiance (i.e., $T^{\min}$ and $T^{\max}$), and the means and variances of the initial gain and bias. However, in practice, these parameters may not be known *a priori*, or they may be known up to some uncertainty (i.e., they may be known probabilistically). In Subsection 2.B, we derive a technique for the adaptive estimation of the gain and bias that is robust with respect to uncertainties associated with the system parameters, which we represent by the vector $\boldsymbol{\theta} \triangleq (\alpha, \beta, T^{\min}, T^{\max}, \bar{A}_0, \sigma_{A_0}^2, \bar{B}_0, \sigma_{B_0}^2)$. This extension is the main contribution of this paper.

B. Multiple-Model Adaptive Estimator

We now introduce the random version, $\boldsymbol{\Theta}$, of the system-parameter vector $\boldsymbol{\theta}$ described above. We will assume that $\boldsymbol{\Theta}$ assumes its values from a finite set $\Omega = \{\boldsymbol{\theta}_1, \ldots, \boldsymbol{\theta}_N\}$, with true *a priori* probabilities $p_{\boldsymbol{\theta}_q} \triangleq \mathsf{P}\{\boldsymbol{\Theta} = \boldsymbol{\theta}_q\}$, $q = 1, \ldots, N$, which are unknown to the user. Throughout, we assume that we have at our disposal N KFs, one for each possible realization of $\boldsymbol{\Theta}$. In what follows, we develop a recursion to estimate these priors from the data.

According to Sims *et al.*,[18] to develop the MMAE estimator at the kth block, it is required that we first find the form of the minimum-mean-square-error estimator of the state $\mathbf{X}_k$ based on both the measurements $\mathbf{Y}_1, \ldots, \mathbf{Y}_k$ and the set Ω. Clearly, this estimator is given by the conditional expectation $\hat{\hat{\mathbf{X}}}_k = \mathsf{E}[\mathbf{X}_k | \mathbf{Y}_1, \ldots, \mathbf{Y}_k]$. If we use the smoothing property of conditional expectations, we obtain

$$\begin{aligned} \hat{\hat{\mathbf{X}}}_k &= \mathsf{E}[\mathsf{E}[\mathbf{X}_k | \mathbf{Y}_1, \ldots, \mathbf{Y}_k, \boldsymbol{\Theta}] | \mathbf{Y}_1, \ldots, \mathbf{Y}_k] \\ &= \mathsf{E}[\hat{\mathbf{X}}_k(\boldsymbol{\Theta}) | \mathbf{Y}_1, \ldots, \mathbf{Y}_k] \\ &= \sum_{q=1}^{N} \hat{\mathbf{X}}_k(\theta_q) \mathsf{P}\{\boldsymbol{\Theta} = \boldsymbol{\theta}_q | \mathbf{Y}_1 = \mathbf{y}_1, \ldots, \mathbf{Y}_k = \mathbf{y}_k\}, \end{aligned} \tag{11}$$

where $\hat{\mathbf{X}}_k(\theta_q) \triangleq \mathsf{E}[\mathbf{X}_k | \mathbf{Y}_1, \ldots, \mathbf{Y}_k, \boldsymbol{\Theta} = \boldsymbol{\theta}_q]$ is the estimate of $\mathbf{X}_k$ generated by the KF according to the qth model and $\hat{p}_{\boldsymbol{\theta}_q | \mathbf{y}_k} \triangleq \mathsf{P}\{\boldsymbol{\Theta} = \boldsymbol{\theta}_q | \mathbf{Y}_1 = \mathbf{y}_1, \ldots, \mathbf{Y}_k = \mathbf{y}_k\}$ is the *a posteriori* probability that the qth model is the true model, given that we observe data up to time k. Note that $\hat{\mathbf{X}}_k(\boldsymbol{\theta}_q)$ in Eq. (11) is calculated precisely from the KF described in Subsection 2.A with $\boldsymbol{\theta}_q$ taken as the vector comprising the model parameters. It can be seen from Eq. (11) that the estimate $\hat{\hat{\mathbf{X}}}_k$ is a weighted sum of N individual and independently calculated estimates for each model.

We now describe how to compute $\hat{p}_{\boldsymbol{\theta}_q | \mathbf{y}_k}$ iteratively. [In what follows, we will use the following notation: if $\mathbf{U} \triangleq (U_1, \ldots, U_k)$ is a continuous random vector and D is a discrete random variable, then by the joint probability density function of $\mathbf{U}$ and D, $f_{U_1,\ldots,U_k,D}(u_1, \ldots, u_k, d)$, we mean $\lim_{\|(\delta_1,\ldots,\delta_k)\| \to 0} \mathsf{P}\{u_1 \leq U_1 < u_1 + \delta_1, \ldots, u_k \leq U_k < u_k + \delta_k, D = d\}$.] Following the procedure given by Sims *et al.*,[18] we utilize Bayes's rule and the law of total probability to obtain

$$\begin{aligned} \hat{p}_{\boldsymbol{\theta}_q | \mathbf{y}_k} &= \frac{f_{\boldsymbol{\Theta},\mathbf{Y}_1,\ldots,\mathbf{Y}_k}(\boldsymbol{\theta}_q, \mathbf{y}_1, \ldots, \mathbf{y}_k)}{f_{\mathbf{Y}_1,\ldots,\mathbf{Y}_k}(\mathbf{y}_1, \ldots, \mathbf{y}_k)} = \frac{f_{\mathbf{Y}_k|\mathbf{Y}_1,\ldots,\mathbf{Y}_{k-1},\boldsymbol{\Theta}}(\mathbf{y}_k | \mathbf{y}_1, \ldots, \mathbf{y}_{k-1}, \boldsymbol{\theta}_q) \hat{p}_{\theta_q|\mathbf{y}_{k-1}} f_{\mathbf{Y}_1,\ldots,\mathbf{Y}_{k-1}}(\mathbf{y}_1, \ldots, \mathbf{y}_{k-1})}{f_{\mathbf{Y}_k|\mathbf{Y}_1,\ldots,\mathbf{Y}_{k-1}}(\mathbf{y}_k | \mathbf{y}_1, \ldots, \mathbf{y}_{k-1}) f_{\mathbf{Y}_1,\ldots,\mathbf{Y}_{k-1}}(\mathbf{y}_1, \ldots, \mathbf{y}_{k-1})} \\ &= \frac{f_{\mathbf{Y}_k|\mathbf{Y}_1,\ldots,\mathbf{Y}_{k-1},\boldsymbol{\Theta}}(\mathbf{y}_k | \mathbf{y}_1, \ldots, \mathbf{y}_{k-1}, \boldsymbol{\theta}_q)}{f_{\mathbf{Y}_y|\mathbf{Y}_1,\ldots,\mathbf{Y}_{k-1}}(\mathbf{Y}_k | \mathbf{y}_1, \ldots, \mathbf{y}_{k-1})} \hat{p}_{\boldsymbol{\theta}_q|\mathbf{y}_{k-1}} = \frac{f_{\mathbf{Y}_k|\mathbf{Y}_1,\ldots,\mathbf{Y}_{k-1},\boldsymbol{\Theta}}(\mathbf{y}_k | \mathbf{y}_1, \ldots, \mathbf{y}_{k-1}, \boldsymbol{\theta}_q)}{\sum_{d=1}^{N} f_{\mathbf{Y}_k|\mathbf{Y}_1,\ldots,\mathbf{Y}_{k-1},\boldsymbol{\Theta}}(\mathbf{y}_k | \mathbf{y}_1, \ldots, \mathbf{y}_{k-1}, \boldsymbol{\theta}_d) \hat{p}_{\boldsymbol{\theta}_d|\mathbf{y}_{k-1}}} \hat{p}_{\boldsymbol{\theta}_q|\mathbf{y}_{k-1}}. \end{aligned} \tag{12}$$

Equation (12) shows that the recursions are a function of the conditional density function $f_{\mathbf{Y}_k|\mathbf{Y}_1,\ldots,\mathbf{Y}_{k-1},\boldsymbol{\Theta}}(\mathbf{y}_k | \mathbf{y}_1, \ldots, \mathbf{y}_{k-1}, \boldsymbol{\theta}_q)$. In this paper, we use the equiprobable initial condition $\hat{p}_{\boldsymbol{\theta}_q|\mathbf{y}_0} \equiv 1/N$. The convergence of the above recursion is established in Subsection 2.C.

The conditional density function $f_{\mathbf{Y}_k|\mathbf{Y}_1,\ldots,\mathbf{Y}_{k-1},\boldsymbol{\Theta}} \times (\mathbf{y}_k | \mathbf{y}_1, \ldots, \mathbf{y}_{k-1}, \boldsymbol{\theta}_q)$ can be easily found.[18] From Eq. (3), it can be seen that $\mathbf{Y}_k(\boldsymbol{\theta}_q)$ is the sum of two Gaussian random variables; therefore, $\mathbf{Y}_k(\boldsymbol{\theta}_q)$ is also Gaussian. Furthermore, the first- and second-order statistics can be computed in terms of the system's parameters of each model and standard formulas for the moments for linear transformations of Gaussian random vectors. In particular, the conditional mean of the vector $\mathbf{Y}_k(\boldsymbol{\theta}_q)$, given $\mathbf{Y}_1, \ldots, \mathbf{Y}_{k-1}$ and $\boldsymbol{\Theta} = \boldsymbol{\theta}_q$, is[18]

$$\mathsf{E}[\mathbf{Y}_k | \mathbf{Y}_1, \ldots, \mathbf{Y}_{k-1}, \boldsymbol{\theta}_q] \equiv \hat{\mathbf{Y}}_k^-(\boldsymbol{\theta}_q) = \bar{\mathbf{H}}(\boldsymbol{\theta}_q) \boldsymbol{\Phi}(\boldsymbol{\theta}_q) \hat{\mathbf{X}}_{k-1}(\boldsymbol{\theta}_q),$$

which is the *a priori* estimate of $\hat{\mathbf{Y}}_{\mathbf{k}}$ based on the qth model. In addition, the conditional covariance matrix of $\mathbf{Y}_k(\boldsymbol{\theta}_q)$ is given by[18]

$$\mathsf{E}[(\mathbf{Y}_k(\boldsymbol{\theta}_q) - \hat{\mathbf{Y}}_k(\boldsymbol{\theta}_q)^-)(\mathbf{Y}_k(\boldsymbol{\theta}_q) - \hat{\mathbf{Y}}_k(\boldsymbol{\theta}_q)^-)^T] = \mathbf{C}_k(\boldsymbol{\theta}_q).$$

Thus,

$$f_{\mathbf{Y}_k|\mathbf{Y}_1,\ldots,\mathbf{Y}_{k-1},\boldsymbol{\Theta}}(\mathbf{y}_k|\mathbf{y}_1,\ldots,\mathbf{y}_{k-1},\boldsymbol{\theta}_q) = \frac{\exp\left\{-\frac{1}{2}[\mathbf{y}_k - \hat{\mathbf{Y}}_k^-(\boldsymbol{\theta}_q)]^T\mathbf{C}_k(\boldsymbol{\theta}_q)^{-1}[\mathbf{y}_k - \hat{\mathbf{Y}}_k^-(\boldsymbol{\theta}_q)]\right\}}{\sqrt{2\pi|\mathbf{C}_k(\boldsymbol{\theta}_q)|}}. \quad (13)$$

In summary, the MMAE method consists of a bank of N independent KFs running in parallel, where each filter corresponds to one of the N candidate models. At each kth block, the bank produces N different estimates, $\hat{\mathbf{X}}_k(\boldsymbol{\theta}_q)$, $q=1,\ldots,N$, of the state vector. Each filter also computes its version of the *a posteriori* probability density function of the data given by Eq. (13). The centralized part of the algorithm computes the *a posteriori* conditional probabilities using the iteration (12) and the initial condition $\hat{p}_{\boldsymbol{\theta}_q|\mathbf{y}_0} \equiv 1/N$. Finally, the estimate of the state at the kth block is calculated using Eq. (11). One of the attractive features of the MMAE is that all the quantities required by Eqs. (12) and (13) are already computed by the normal execution of the KFs independently of the conditional probabilities.

C. Convergence

It has been shown that if the output residual error for each model, $\mathbf{r}_k(\boldsymbol{\theta}_q) \triangleq \mathbf{Y}_k - \hat{\mathbf{Y}}_k(\boldsymbol{\theta}_q)$, is asymptotically wide-sense stationarity (WSS), then two key convergence properties hold.[20,21] First, if $p_{\boldsymbol{\theta}_q} = \delta_{\boldsymbol{\theta}_q,\boldsymbol{\theta}^*}$, for some $\boldsymbol{\theta}^* \in \Omega$ (here $\delta_{m,n}$ is the Kronecker Dirac), then $\hat{p}_{\boldsymbol{\theta}^*|\mathbf{y}_k} \to 1$ as $k\to\infty$, or, equivalently, $\hat{p}_{\boldsymbol{\theta}_q|\mathbf{y}_k} \to p_{\boldsymbol{\theta}_q}$, which means that the correct model is eventually selected as the iteration described by Eq. (12) evolves. The second property states that if $\boldsymbol{\theta}^* \notin \Omega$, then $\hat{p}_{\boldsymbol{\theta}_q|\mathbf{y}_k} \to \tilde{p}_{\boldsymbol{\theta}_q}$, as $k\to\infty$, for some probability mass function $\tilde{p}_{\boldsymbol{\theta}_q}$ with the property that if $\tilde{\boldsymbol{\theta}} = \operatorname{argmax}_{q=1,\ldots,N}\tilde{p}_{\boldsymbol{\theta}_q}$, then $|\tilde{\boldsymbol{\theta}} - \boldsymbol{\theta}^*| \leq |\tilde{\boldsymbol{\theta}} - \boldsymbol{\theta}_q|$, for all $\boldsymbol{\theta}_q \neq \tilde{\boldsymbol{\theta}}$. This implies that the candidate model that is closest to the true model receives the highest weight in the composite estimate.

Indeed, a straightforward (but tedious) calculation shows that the expected value of the sequence $\mathbf{r}_k(\boldsymbol{\theta}_q)$ is zero. Moreover, by utilizing the fact that the elements of the sequence $\mathbf{H}_k$ are mutually independent, we can calculate the autocorrelation function of the sequence as

$$\mathsf{E}[\mathbf{r}_k(\boldsymbol{\theta}_q)\mathbf{r}_{k+n}(\boldsymbol{\theta}_q)^T] = \bar{\mathbf{H}}(\boldsymbol{\theta}_q)(\boldsymbol{\Phi}(\boldsymbol{\theta}_q)\mathbf{P}_{n-1}(\boldsymbol{\theta}_q)\boldsymbol{\Phi}^T(\boldsymbol{\theta}_q) + \mathbf{Q}(\boldsymbol{\theta}_q) + \mathbf{M}(\boldsymbol{\theta}_q)\mathbf{M}^T(\boldsymbol{\theta}_q))\bar{\mathbf{H}}^T(\boldsymbol{\theta}_q), \quad (14)$$

which is independent of k. Hence, the residual errors of the filter are actually WSS (which, of course, implies asymptotic WSS), and the convergence of the proposed algorithm is established.[21]

3. APPLICATION TO IMAGE SEQUENCES WITH SIMULATED NONUNIFORMITY NOISE

The MMAE algorithm was tested using blocks of clean IR image sequences corrupted by simulated NU noise exhibiting drift in the gain and bias. For the purpose of this study, the noiseless IR imagery was obtained by applying a two-point calibration to real IR imagery. Specifically, we employed three and four blocks of IR data, each of them formed by 500 frames of 128×128 pixels, and every pixel was quantized to 16 bits.

The simulation of imagery with NU noise was done as follows. Initially, i.e., for the first block of frames, a random gain and bias were generated independently for each pixel from Gaussian distributions with mean values of 1 and zero, respectively. The level of NU introduced to the initial block is set by varying the variance of the gain and the bias. In addition, we simulated the drift in the gain and the bias from block to block by using the Gauss–Markov model described in Subsection 2.A with predefined parameters α and β. The temporal noise was simulated using a zero-mean Gaussian random variable, which is uncorrelated with both the gain and the bias. Our Monte Carlo calculations were based on 100 trials for each set of parameters studied.

The performance of the MMAE was evaluated by means of the mean square error (MSE) between the true and the estimated values of the gain and the bias. The NUC capability was then examined in terms of the root-mean-square error (RMSE) between the original and the corrected imagery. (The NUC is performed by subtracting the estimated biases from the corrupted data and dividing the outcome by the estimated gains.) Given that $\boldsymbol{\Theta}$, the discrete random parameter vector, includes in its components several different parameters that produce different effects over the estimates, we will study each component of $\boldsymbol{\Theta}$ independently. First, we will consider the capability of the MMAE algorithm to adapt to the drift in the gain and bias. Later, we will study the behavior of the MMAE when changes occur in the initial condition or the observation matrix as they correspond to different combinations for the discrete random vector $\boldsymbol{\Theta}$.

A. Estimation of the Drift in the Gain and the Bias

We conducted experiments to test the performance of the MMAE to estimate and track the drift of the NU parameters by using a bank of five KFs. In our first experiment we simulated a constant and low amount of drift in the NU parameters: $\alpha_k=\beta_k=0.95$, $k=1,2,3$. The KFs were designed considering that all models had the actual parameters for $T^{\min}, T^{\max}, \bar{A}_0, \sigma^2_{A_0}, \bar{B}_0, \sigma^2_{B_0}$. The different values of $\alpha(\boldsymbol{\theta}_q)$ and $\beta(\boldsymbol{\theta}_q)$, for each model, used in the experiments are shown in the first column of Table 1. Note that

Table 1. Spatial Average of the *a posteriori* Conditional Probabilities $\hat{p}_{\boldsymbol{\theta}_q|\mathbf{y}_k}$ for Each Model[a]

Model $q:(\alpha=\beta)$	$\hat{p}_{\boldsymbol{\theta}_q|\mathbf{y}_1}$	$\hat{p}_{\boldsymbol{\theta}_q|\mathbf{y}_2}$	$\hat{p}_{\boldsymbol{\theta}_q|\mathbf{y}_3}$
1: 0.90	0.1999	0.2028	0.1925
2: 0.92	0.1954	0.2173	0.2390
3: 0.88	0.2045	0.1857	0.1545
4: 0.94	0.1910	0.2266	0.2902
5: 0.86	0.2092	0.1676	0.1238

[a]In this example the true parameter is not a member of the parameter space Ω; however, the fourth model ($\boldsymbol{\theta}_4$) is closest to the true parameter set.

Table 2. NUC Performance Parameters Obtained by the MMAE for the Experiment Corresponding to Table 1

Model ($\alpha=\beta$)	MSE_{A_1}	MSE_{B_1}	RMSE_1	MSE_{A_2}	MSE_{B_2}	RMSE_2	MSE_{A_3}	MSE_{B_3}	RMSE_1
1: 0.90	0.0445	0.3692	0.4463	0.0288	0.2018	0.3742	0.0193	0.1481	0.3428
2: 0.92	0.0443	0.3690	0.4462	0.0286	0.2012	0.3739	0.0192	0.1479	0.3426
3: 0.88	0.0448	0.3700	0.4466	0.0286	0.2022	0.3744	0.0196	0.1492	0.3431
4: 0.94	0.0443	0.3690	0.4461	0.0282	0.2004	0.3737	0.0190	0.1477	0.3425
5: 0.86	0.0441	0.3688	0.4456	0.0293	0.2029	0.3745	0.0197	0.1500	0.3432

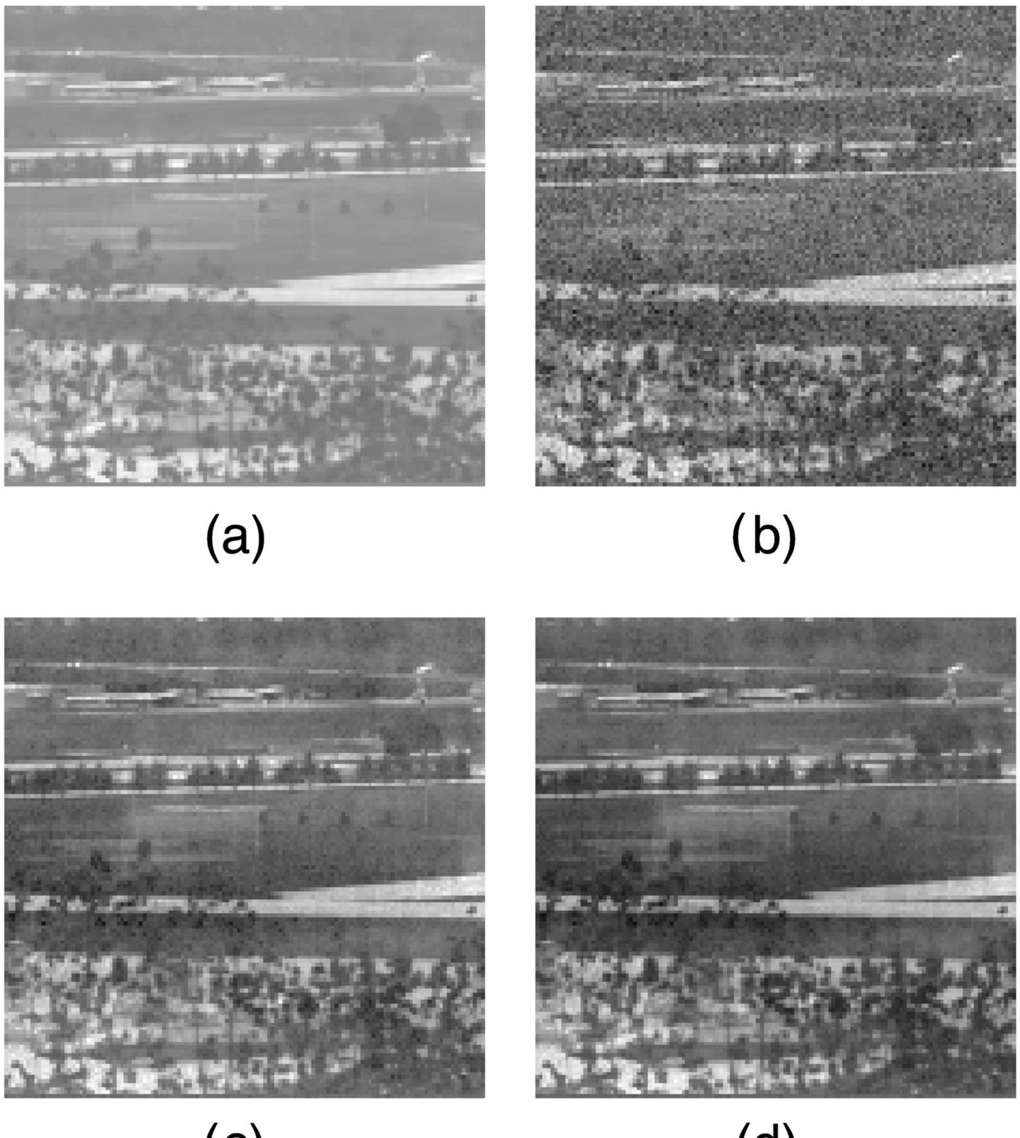

Fig. 1. Image frame 500 from the third block ($k=3$) (a) true image, (b) noisy image, (c) corresponding corrected version of the noisy image obtained by the first KF of the bank, (d) corrected version of the noisy image obtained by the fourth KF.

the fourth model is the closest one to the true model.

The results of the experiment are shown in Table 1. It can be seen that the fourth model achieves the greatest probability after the first block. Note that, despite the fact that the parameters vary only slightly between models, the MMAE is able to identify the model that is closest to the true model. Also, as shown in Table 2, the KF corresponding to the fourth model performs better than the other KFs in estimating the NU parameters. A visual inspection of the corrected imagery (see Fig. 1) also shows that the levels of residual NU present in the corrected images shown in Figs. 1(c) and 1(d), obtained by models 1 and 4, respectively, are very low compared with the noisy IR image shown in Fig. 1(b). Recall that the estimate of the MMAE algorithm corresponds to the weighted superposition of all the estimates rendered by each KF; therefore, in this case, the corrected image achieved by the MMAE looks closer to Fig. 1(d) than Fig. 1(c).

In the second experiment we assign the actual set of parameters ($\alpha=\beta=0.95$) to the second model. Starting with $\hat{p}_{\boldsymbol{\theta}_q|\mathbf{y}_0}=0.2$, $q=1,\ldots,5$, the *a posteriori* probabilities of model 2 being selected are $\hat{p}_{\boldsymbol{\theta}_2|\mathbf{y}_1}=0.2923$, $\hat{p}_{\boldsymbol{\theta}_2|\mathbf{y}_2}=0.8638$, and $\hat{p}_{\boldsymbol{\theta}_2|\mathbf{y}_3}=0.9237$. This demonstrates that the MMAE is not only able to identify the correct model but also converge to it fast.

In the third experiment we used $\alpha=\beta=0.95$ in the first two blocks and then switched to $\alpha=\beta=0.80$ in the third and fourth blocks. This scenario models the realistic case when the drift is time variant (e.g., when the ambient temperature of the sensor changes abruptly); it also demonstrates the ability of the MMAE to adapt to changes and track the drift in the gain and bias. In Table 3 we show $\hat{p}_{\boldsymbol{\theta}_q|\mathbf{y}_k}$ obtained for each model as a function of the block number. The results show that the MMAE selects the correct (i.e., first) model in the second block and then it selects the correct model (second) for blocks 3 and 4 in the fourth block.

B. Exploiting Spatial Dependencies

Recall that the only parameters in $\boldsymbol{\Theta}$ that can vary from detector to detector are the drift parameters, α and β; all other parameters, viz., the initial statistics of the gain and bias, as well as the irradiance range, are assumed uniform spatially. However, from our experience we have seen that the amount of drift in the gain and bias is more or less similar for all photodetectors. This observation suggests that it would be plausible to assume, at least locally, that the drift parameters exhibit a high level of spatial dependency. In other words, the probability mass function of the random vector $\boldsymbol{\Theta}$ may be assumed fixed over a certain neighborhood of detectors. Clearly, this feature can be exploited to enhance the computational efficiency of the MMAE by requiring the calculation of the *a posteriori* probabilities $\hat{p}_{\boldsymbol{\theta}_q|\mathbf{y}_k}$ for only a subsample of detectors.

To do so, the MMAE is first restricted to spatially downsampled imagery, and the probabilities $\hat{p}_{\boldsymbol{\theta}_q|\mathbf{y}_k}$ are computed for the reduced subset of detectors. Next, the *a posteriori* probabilities for the remaining detectors are approximated by means of spatial interpolation (we used zeroth-order interpolation in our calculations). The gain and bias are then estimated for each detector by using the MMAE according to the subsampled or interpolated probabilities. Indeed, Fig. 2 shows that the mean (over all pixels and all frames in one block) RMSE is almost independent of the downsampling factor, which justifies our spatial dependency assumption regarding the drift parameters. The figure also shows the significant reduction in computing time, which scales with the downsampling factor. Evidently, the proposed zeroth-order interpolation method is just one simple way of exploiting the spatial dependencies. If for some kind of application we need to impose spatial continuity on the sensor, then, for example, we should consider Markov–random–field-based inference algorithms that achieve efficient solutions to the problem of imposing smoothness across the sensor.[22]

Table 3. Spatial Average of the *a posteriori* Conditional Probabilities, $\hat{p}_{\boldsymbol{\theta}_q|\mathbf{y}_k}$, for Each Model When the MMAE is Tracking the Artificial NU Added to a Sequence of Four Blocks of Data[a]

Model ($\alpha=\beta$)	$\hat{p}_{\theta_q\|\mathbf{y}_1}$	$\hat{p}_{\theta_q\|\mathbf{y}_2}$	$\hat{p}_{\theta_q\|\mathbf{y}_3}$	$\hat{p}_{\theta_q\|\mathbf{y}_4}$
1: 0.95	0.1662	0.5963	0.6030	0.4721
2: 0.80	0.1965	0.3636	0.3647	0.4794
3: 0.35	0.1796	0.0098	0.0097	0.0100
4: 0.55	0.2428	0.0203	0.0128	0.0278
5: 0.40	0.2150	0.0100	0.0097	0.0107

[a] In the first two blocks, the actual values are $\alpha=\beta=0.95$, and, in the third and four blocks, $\alpha=\beta=0.80$.

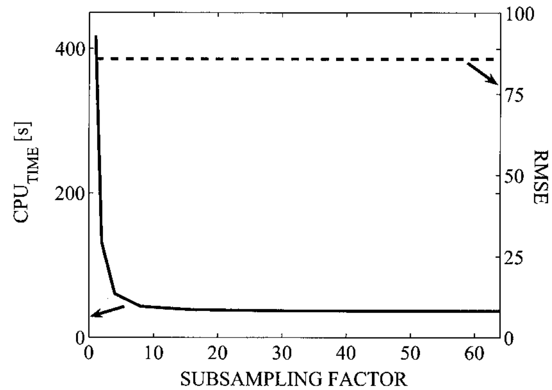

Fig. 2. Computing time required by the MMAE and its corresponding RMSE obtained versus the subsampling factor used to calculate the *a posteriori* conditional probabilities.

4. APPLICATION TO REAL INFRARED IMAGE SEQUENCES

In this section, the MMAE algorithm is applied to two sets of raw IR data collected using different IR cameras. The first set corresponds to five videos of terrestrial midwave IR (3–5 μm) imagery, collected using a 128×128 InSb FPA cooled camera (Amber Model AE-4128). The IR videos were collected at different hours of the same day (6:30 a.m., 8 a.m., 9:30 a.m., 11 a.m., and 1 p.m.), each video contained 1000 frames captured at a rate of 30 frames/s (fps), and each pixel was quantized in 16 bit integers. The second set also corresponds to terrestrial data, in the range of 8–12 μm, and was collected using an HgCdTe FPA cooled camera (CEDIP Jade Model) that outputs frames of 320×240 pixels, quantized in 14 bit integers. The data were acquired at 30 fps and then subsampled in time by a factor of 10, to obtain four subsampled videos with 500 frames per block. Unlike the InSb camera, the range of the data acquired by the HgCdTe camera is [5961,8934], which is much smaller than the entire available range. Finally, the blocks of frame videos were collected at 2 p.m., 2:30 p.m., 2:45 p.m., and 3:05 p.m., all taken in the same day.

A. Uncertainties in the Drift of the Nonuniformity Parameters

Recall that the key objective of the proposed MMAE technique is to adaptively track the level of drift in the gain, which would include identifying the true values of the parameters α and β. To demonstrate this capability for the two sets of IR video sequences, the video sequences were sorted in time, and we set $\alpha=\beta$ to be 0.50, 0.60, 0.70, 0.8, and 0.9 for models 1 to 5, respectively, and for both sets of IR imagery. All the other parameters of the model were set to be the same for the five KFs.

From Eq. (1), the initial conditions $\bar{A}_0$, $\bar{B}_0$, $\sigma^2_{A_0}$, and $\sigma^2_{B_0}$ for the gain and the bias must satisfy the relations

$$\bar{Y}=\bar{A}_0\bar{T}+\bar{B}_0, \tag{15}$$

$$\sigma^2_Y=\sigma^2_{A_0}(\sigma^0_T+\bar{T}^2)+\bar{A}^2_0\sigma^2_T+\sigma^2_{B_0}, \tag{16}$$

where $\bar{Y}$ and σ^2_Y are, respectively, the empirical mean and variance of the readout data (across all detectors and frames in the first block) and $\bar{T}=(T^{\max}+T^{\min})/2$ and $\sigma^2_T=(T^{\max}-T^{\min})^2/12$ are, respectively, the theoretical mean and variance of the irradiance. Clearly, additional assumptions need to be made to determine the four initial conditions. Our experience indicates that selecting $\bar{A}_0=1$ produces corrected images in the same dynamic range of the readout data. Moreover, a reasonable assumption regarding the gain NU is that $\sigma^2_{A_0}\approx 0.05\bar{A}^2_0$. Consequently, in the case of the IR data collected with the InSb FPA, for which $T^{\min}=0$ and $T^{\max}=65\,535$, we obtain (after rounding) $\bar{B}_0=-4000$ and $\sigma^2_{B_0}=3300$. Note that the assumptions imposed on the initial condition are not restrictive but are necessary because different IR cameras quantize the images using different numbers of bits and/or different dynamic ranges.

After running the MMAE algorithm with the above initial conditions, we obtain the following maximum *a posteriori* conditional probabilities (over the five models) at each time: $\hat{p}_{\boldsymbol{\theta}_5|\mathbf{y}_1}=0.6168$, $\hat{p}_{\boldsymbol{\theta}_4|\mathbf{y}_2}=0.7792$, $\hat{p}_{\boldsymbol{\theta}_4|\mathbf{y}_3}=0.9933$, $\hat{p}_{\boldsymbol{\theta}_4|\mathbf{y}_4}=0.9997$, and $\hat{p}_{\boldsymbol{\theta}_4|\mathbf{y}_5}=1$, which suggest that the correct model is the fourth one (namely, $\alpha=\beta=0.8$). The *a posteriori* conditional probabilities show that the amount

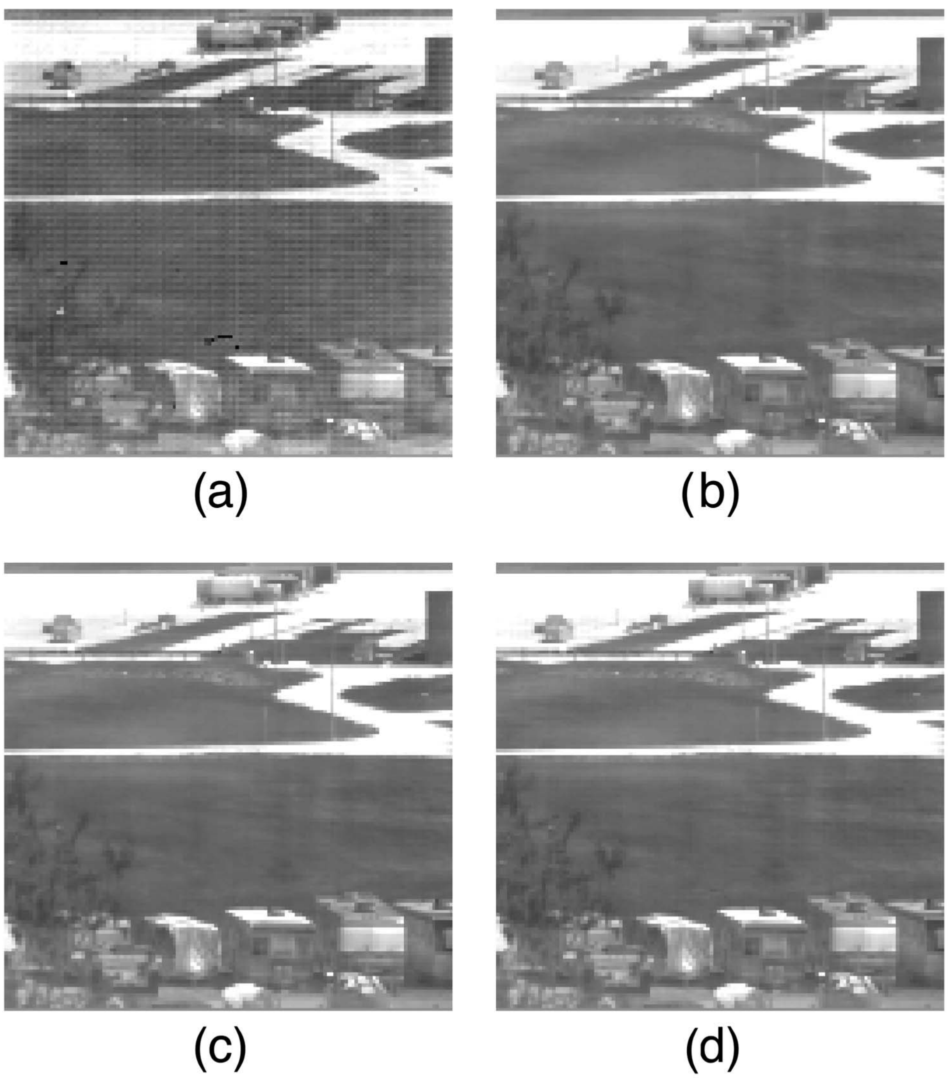

Fig. 3. (a) Sample raw image of the fifth block ($k=5$) taken from the InSb data set, (b) corrected version of the raw image obtained by the first KF, (c) corrected image obtained by the second KF, (d) corrected frame obtained by the fourth KF.

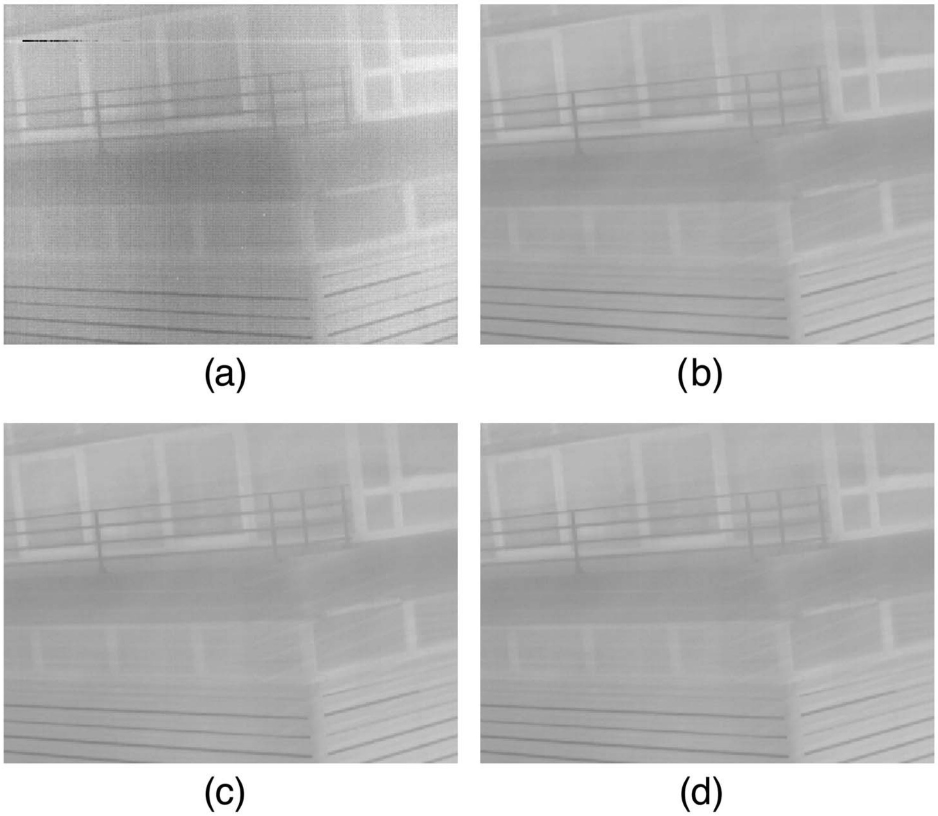

Fig. 4. (a) Sample raw image of the first block ($k=1$) taken from the HgCdTe data set, (b) corrected version of the raw image obtained by the first KF, (c) corrected frame obtained by the fourth KF, (d) corrected frame obtained by the fifth KF. Note that the image in (d), which has the highest *a posteriori* probability, offers a slight advantage in performing NUC.

of drift in the gain and the bias is slow (α and β tend to 1), which is in agreement with the MMAE estimates obtained for the gain and the bias: $\hat{A}_1=0.6143$, $\hat{A}_2=0.8510$, $\hat{A}_3=0.8200$, $\hat{A}_4=0.8127$, and $\hat{A}_5=0.8383$; $\hat{B}_1=-9032$, $\hat{B}_2=-3602$, $\hat{B}_3=-2055$, $\hat{B}_4=-1807$, and $\hat{B}_5=-1443$.

For the set of data corresponding to the HgCdTe camera, the MMAE's initial conditions are given by $\bar{A}_0=1$, $\bar{B}_0=-1200$, $\sigma^2_{A_0}=0.05$, $\sigma^2_{B_0}=1600$, $T^{\min}=5961$, and $T^{\max}=8934$. The estimated gain and bias for this set are $\hat{A}_1=1.2771$, $\hat{A}_2=1.1827$, $\hat{A}_3=1.1521$, and $\hat{A}_4=1.1458$; $\hat{B}_1=-991$, $\hat{B}_2=-2061$, $\hat{B}_3=-2165$, and $\hat{B}_4=-1691$. The results obtained for the highest *a posteriori* conditional probabilities are $\hat{p}_{\boldsymbol{\theta}_5|\mathbf{y}_1}=0.3598$, $\hat{p}_{\boldsymbol{\theta}_5|\mathbf{y}_2}=0.3985$, $\hat{p}_{\boldsymbol{\theta}_5|\mathbf{y}_3}=0.5501$, and $\hat{p}_{\boldsymbol{\theta}_5|\mathbf{y}_4}=0.5897$, which indicate that the model closest to the correct model is the fifth model (namely, $\alpha=\beta=0.9$).

Figure 3(a) shows a sample raw frame, at $k=5$, for the InSb data. Figures 3(b)–3(d) correspond to filtered images computed by the first, second, and fourth KFs, respectively (the images corresponding to the other modes are not shown). The NUC obtained for the IR sequence was somehow satisfactory. Further, it can be also seen that the MMAE compensates for the dead pixels that appear in the real imagery. However, a small amount of ghosting appears in the corrected images. Figure 4(a) shows a raw frame for $k=1$ taken from the HgCdTe data. Figures 4(b)–4(d) are the corresponding filtered versions of Fig. 4(a), corrected using the first, the fourth, and the fifth KF estimators, respectively. In this example, no ghosting artifacts were observed.

B. Uncertainties in the Irradiance Range and the Initial Condition of the Gauss–Markov Model

We now study the dependence of the MMAE on the mean initial gain $\bar{A}_0$ and bias $\bar{B}_0$ while fixing the reaming model parameters. According to previous results, we set $\alpha=\beta=0.8$ for all the models in the InSb data and $\alpha=\beta=0.9$ for the HgCdTe data. Further, we maintain the same values for $T^{\min}$, $T^{\max}$, $\sigma^2_{A_0}$, and $\sigma^2_{B_0}$ as used in Subsection 4.A. We propose the following candidate values for the mean gain $\bar{A}_0$ for both cameras: 0.6, 0.7, 0.8, 0.9, and 1.0 in models 1 to 5, respectively. According to Eq. (15), the corresponding candidate values for the mean bias become −43 000, −28 000, −16 000, −7800, and 0 for the InSb data and −2409, −1684, −959, −234, and −490 for the HgCdTe data. Next, we executed the MMAE and found that the maximum (over all models) *a posteriori* conditional probabilities obtained at each kth time for the InSb data are $\hat{p}_{\boldsymbol{\theta}_3|\mathbf{y}_1}=0.2218$, $\hat{p}_{\boldsymbol{\theta}_2|\mathbf{y}_2}=0.3695$, $\hat{p}_{\boldsymbol{\theta}_3|\mathbf{y}_3}=0.4270$, $\hat{p}_{\boldsymbol{\theta}_3|\mathbf{y}_4}=0.4285$, and $\hat{p}_{\boldsymbol{\theta}_3|\mathbf{y}_5}=0.5331$. For the HgCdTe data, the results are $\hat{p}_{\boldsymbol{\theta}_4|\mathbf{y}_1}=0.2214$, $\hat{p}_{\boldsymbol{\theta}_5|\mathbf{y}_2}=0.3444$, $\hat{p}_{\boldsymbol{\theta}_5|\mathbf{y}_3}=0.5332$, and $\hat{p}_{\boldsymbol{\theta}_5|\mathbf{y}_4}=0.7102$. The results indicate that the best choice for the gain (bias) for the InSb and HgCdTe cameras are 0.8 (−16 000) and 1.0 (−490), respectively.

Finally, we also performed experiments to determine the best range for the input irradiance while keeping all other system parameters fixed. Our results indicate that the MMAE tends to select the range that is consistent with data. More precisely, for a fixed mean gain $\bar{A}_0$ and mean bias $\bar{B}_0$, the selected range $[T^{\min}, T^{\max}]$ would contain the data range after the data are shifted by the bias and scaled by the mean gain. This conclusion is consistent with the maximum-likelihood estimator of a uniformly distributed random variable (the irradiance in this case) from linearly transformed samples of it.

C. Implementation Issues

A real-time implementation of the MMAE algorithm has to consider the following requirements imposed by the algorithm: a bank of N KFs, a common input buffer to store the incoming block of observations, and memory to store the estimates of the gain and the bias, the *a posteriori* probabilities, and the weighting factors. It should be noted that the bank of KFs is not required to be implemented in parallel. For the case of the input buffer, in Refs. 12 and 13 we showed that at least 500 frames are needed to obtain the estimates of the gain and the bias. The estimates of the gain and the bias, the *a posteriori* probabilities, and the weighting factors required saving $3(N+1)$ matrices of floating-point numbers. Finally, the MMAE also required to saving N 2×2 matrices corresponding to the error covariance matrices of each KF.

5. CONCLUSIONS

In this paper we developed a scene-based method for estimating the gain and bias matrices in infrared focal-plane arrays that is robust with respect to uncertainties in the sensor-model parameters. These include uncertainties in the spatial statistics of the fixed-pattern noise (namely, uncertainties in the statistics of the gain and bias) as well as the uncertainties in the drift in the gain and bias. The method is based on the multimodel Kalman filter, which consists of a bank of our Kalman filters, one for each set of candidate system parameters, in conjunction with a iterative algorithm that adaptively weighs each output of the bank of filters and computes an aggregate estimator of the gain and bias. Experiments with infrared imagery with simulated fixed-pattern noise demonstrated that the proposed method not only is able to select the best model from a set of candidate models but is also able to adapt to changes in the individual detectors' gains and biases as they drift in time. Our results using real video sequences using InSb and HgCdTe infrared cameras have shown that the estimated gains and biases can be used to perform effective nonuniformity correction to the video sequences over an extended span of time. It should be noted that the success of the proposed methods relies on the constant-statistics assumption,[11] whereby the statistics of the irradiance are assumed to be invariant over all detectors in the array. Finally, it was demonstrated that any spatial dependency in the bias and gain over a neighborhood of detectors can be exploited to save computational resources.

ACKNOWLEDGMENTS

The authors thank Ernest E. Armstrong (OptiMetrics, Inc., USA) and Pierre Potet (CEDIP Infrared Systems, France) for providing portions of the data. The authors also thank the Department of Electrical and Computer Engineering at the University of New Mexico for its support of the Expand Your Engineering Skills (EYES) summer internship program with the Indian Institute of Technology, Kharagpur, India. S. N. Torres acknowledges support by grants Milenio ICM P02-049 and by National Fund for Science and Technology FONDECY 1060894, both from the Chilean government. Finally, the authors thank the reviewers for their helpful comments to improve the presentation of this work.

J. E. Pezoa and M. M. Hayat can be reached by phone, 505-277-0297; fax, 505-277-1439; or e-mail, jpezoa@eece.unm.edu, hayat@ece.unm.edu. S. N. Torres can be reached by phone, 56-41-203005; fax, 56-41-246999, or e-mail, sertorre@udec.cl. Md. S. Rahman can be reached by e-mail at u2ie1004@iitian.iitkgp.ernet.in.

REFERENCES

1. J. Harris and Y.-M. Chiang, "Nonuniformity correction of infrared image sequences using the constant-statistics constraint," IEEE Trans. Image Process. **8**, 1148–1151 (1999).
2. A. Milton, F. Barone, and M. Kruer, "Influence of nonuniformity on infrared focal plane array performance," Opt. Eng. (Bellingham) **24**, 855–862 (1985).
3. J. Mooney, F. Shepherd, W. Ewing, J. Murguia, and J. Silverman, "Responsivity nonuniformity limited performance of infrared staring cameras," Opt. Eng. (Bellingham) **28**, 1151–1161 (1989).
4. D. Perry and E. Dereniak, "Linear theory of nonuniformity correction in infrared staring sensors," Opt. Eng. (Bellingham) **32**, 1854–1859 (1993).
5. H. Zhou, S. Liu, D. Wang, and Y. Cheng, "Solution for the nonuniformity correction of infrared focal plane arrays," Appl. Opt. **44**, 2928–2932 (2005).
6. E. E. Armstrong, M. M. Hayat, R. C. Hardie, S. N. Torres, and B. Yasuda, "Nonuniformity correction for improved registration and high-resolution image reconstruction in IR imagery," in *Applications of Digital Image Processing XXII*, A. G. Tescher, ed., Proc. SPIE **3808**, 150–161 (1999).
7. R. C. Hardie, M. M. Hayat, E. E. Armstrong, and B. Yasuda, "Scene-based nonuniformity correction using video sequences and registration," Appl. Opt. **39**, 1241–1250 (2000).
8. B. Ratliff, M. Hayat, and R. Hardie, "An algebraic algorithm for nonuniformity correction in focal-plane arrays," J. Opt. Soc. Am. A **19**, 1737–1747 (2002).
9. B. Ratliff, M. Hayat, and R. Hardie, "Radiometrically accurate scene-based nonuniformity correction for array sensors," J. Opt. Soc. Am. A **20**, 1890–1899 (2002).
10. B. Ratliff, M. Hayat, and J. Tyo, "Generalized algebraic scene-based nonuniformity correction algorithm," J. Opt. Soc. Am. A **22**, 239–249 (2005).
11. P. Narendra, "Reference-free nonuniformity compensation for IR imaging arrays," in *Smart Sensors II*, D. F. Barbe, ed., Proc. SPIE **252**, 10–17 (1980).
12. S. Torres and M. Hayat, "Kalman filtering for adaptive nonuniformity correction in infrared focal-plane arrays," J. Opt. Soc. Am. A **20**, 470–480 (2003).
13. S. Torres, J. Pezoa, and M. Hayat, "Scene-based nonuniformity correction for focal plane arrays by the method of the inverse covariance form," Appl. Opt. **42**, 5872–5881 (2003).
14. D. Scribner, M. Kruer, and J. Killiany, "Infrared focal plane array technology," Proc. IEEE **79**, 66–85 (1991).

15. D. Scribner, K. Sarkady, M. Kruer, J. Calufield, J. Hunt, M. Colbert, and M. Descour, "Adaptive retina-like preprocessing for imaging detector arrays," in *Proceedings of the IEEE International Conference on Neural Networks* (IEEE, 1993), Vol. 3, pp. 1955–1960.
16. Y.-M. Chiang and J. G. Harris, "An analog integrated circuit for continuous-time gain and offset calibration of sensor arrays," Analog Integr. Circuits Signal Process. **12**, 231–238 (1997).
17. M. Hayat, S. Torres, E. Armstrong, B. Yasuda, and S. Cain, "Statistical algorithm for nonuniformity correction in focal-plane arrays," Appl. Opt. **38**, 772–780 (1999).
18. S. Sims, D. Lianiotis, and D. Magill, "Recursive algorithm for the calculation of the adaptive Kalman filter weighting coefficients," IEEE Trans. Autom. Control **14**, 215–218 (1969).
19. G. C. Holst, *CCD Arrays, Cameras and Displays* (SPIE, 1996).
20. R. Hawkes and J. Moore, "Performance bounds for adaptive estimation," Proc. IEEE **64**, 1143–1150 (1976).
21. B. Anderson and J. Moore, *Optimal Filtering* (Prentice Hall, 1979).
22. M. F. Tappen and W. T. Freeman, "Comparison of graph cuts with belief propagation for stereo, using identical MRF parameters," in *Proceedings of the Ninth IEEE International Conference on Computer Vision* (IEEE, 2003), Vol. 2, pp. 900–907.